# H I Narrow-line Self-absorptions toward the High-mass Star-forming Region G176.51+00.20

Yingjie Li[1] , Ye Xu[1] , Jin-Long Xu[2,3], Dejian Liu[1,4], Jingjing Li[1], Zehao Lin[1,4], Peng Jiang[2,3], Shuaibo Bian[1,4] ,
Chaojie Hao[1,4], and Xiuhui Chen[5]

[1] Purple Mountain Observatory, Chinese Academy of Sciences, Nanjing 210008, People's Republic of China; liyj@pmo.ac.cn, xuye@pmo.ac.cn
[2] National Astronomical Observatories, Chinese Academy of Sciences, Beijing 100101, People's Republic of China
[3] CAS Key Laboratory of FAST, National Astronomical Observatories, Chinese Academy of Sciences, Beijing 100101, People's Republic of China
[4] University of Science and Technology of China, Hefei, Anhui 230026, People's Republic of China
[5] College of Mathematics and Physics, Hunan University of Arts and Science, Changde, Hunan 415300, People's Republic of China

## Abstract

Using the Five-hundred-meter Aperture Spherical radio Telescope (FAST) 19-beam tracking observational mode, high-sensitivity and high-velocity-resolution H I spectral lines have been observed toward the high-mass star-forming region G176.51+00.20. This is a pilot study searching for H I narrow-line self-absorption (HINSA) toward high-mass star-forming regions where bipolar molecular outflows have been detected. This work is confined to the central seven beams of FAST. Two HINSA components are detected in all seven beams, which correspond to a strong CO emission region (SCER; with a velocity of $\sim -18\,\mathrm{km\,s^{-1}}$) and a weak CO emission region (WCER; with a velocity of $\sim -3\,\mathrm{km\,s^{-1}}$). The SCER detected in Beam 3 is probably more suitably classified as a WCER. In the SCER, the HINSA is probably associated with the molecular material traced by the CO. The fractional abundance of HINSA ranges from $\sim 1.1 \times 10^{-3}$ to $\sim 2.6 \times 10^{-2}$. Moreover, the abundance of HINSA in Beam 1 is lower than that in the surrounding beams (i.e., Beams 2 and 4–7). This possible ring could be caused by the ionization of H I or the relatively rapid conversion from H I to $H_2$ in the higher-density inner region. In the WCER (including Beam 3 in the SCER), the HINSA is probably not associated with CO clouds, but with CO-dark or CO-faint gas.

*Unified Astronomy Thesaurus concepts:* Interstellar atomic gas (833); Interstellar abundances (832); Interstellar molecules (849); Star formation (1569); Interstellar dynamics (839); Jets (870)

## 1. Introduction

Stars form in molecular clouds, and it is important for star formation to synthesize molecular $H_2$ from atomic H. However, it is difficult to directly extract individual components from H I emission and correlate them with molecular clouds (Li & Goldsmith 2003; Liu et al. 2022). In such conditions, H I self-absorption (HISA) lines have become a very useful tracer of H I. HISA occurs in environments where cold H I gas is in front of a warmer emission background (e.g., Knapp 1974); such conditions are ubiquitous in the Milky Way (e.g., Heeschen 1955; Gibson et al. 2000; Wang et al. 2020). HISA is associated with both CO-dark clouds and molecular clouds with strong CO emission (e.g., Hasegawa et al. 1983; Gibson et al. 2000; Gibson 2010). H I narrow-line self-absorption (HINSA), a special case of HISA, is usually associated with CO clouds, and its line width is comparable to or smaller than that of CO (see Li & Goldsmith 2003; Goldsmith & Li 2005; Tang et al. 2016; Wang et al. 2020). HINSA has been found to be an excellent tracer of molecular clouds (Li & Goldsmith 2003), and this tight correlation has been confirmed by numerous studies (e.g., Krčo & Goldsmith 2010; Tang et al. 2020; Liu et al. 2022).

Numerous surveys have provided abundant knowledge about the environment and physical properties of the regions producing HINSA. For instance, the detection rate of HINSA is $\sim 77\%$ (Li & Goldsmith 2003) in optically selected dark clouds

(Lee & Myers 1999), $\sim 80\%$ (Krčo & Goldsmith 2010) in molecular cores (Lynds 1962; i.e., the Lynds dark cloud, which has a peak optical extinction of 6 mag or more; see the catalog of dark clouds in), and $\sim 58\%$ (Tang et al. 2020) to $\sim 92\%$ (Liu et al. 2022) in Planck Galactic cold clumps (PGCCs; cold and quiescent clumps in very early evolution stages of star formation; see Planck Collaboration et al. 2011; Wu et al. 2012; Planck Collaboration et al. 2016). These results indicate that HINSA is associated with molecular clouds, especially molecular cores and/or clumps. These papers also constrained the abundance of HINSA, which ranges from $\sim 10^{-4}$ to $\sim 10^{-2}$ (e.g., Krčo & Goldsmith 2010; Tang et al. 2020; Liu et al. 2022); the relationship of the central velocity, line width, and column density between HINSA and the molecular gas traced by $^{12}CO$, $^{13}CO$, OH, etc. (e.g., Li & Goldsmith 2003; Tang et al. 2020; Liu et al. 2022) and the atomic gas traced by C I (e.g., Li & Goldsmith 2003); and even a ring of enhanced HINSA abundance inside a dark molecular cloud (i.e., in B227; see Zuo et al. 2018).

Star-forming regions characterized by molecular outflows have also been incorporated into samples arising from the search for HINSA (e.g., Liu et al. 2022). In this study, the corresponding detection rate of HINSA was only 25% (i.e., one in four sources characterized by molecular outflows). As such, one of our goals is to enlarge the sample of known star-forming regions characterized by molecular outflows. A good choice is the nine regions where outflowing gases traced by $^{12}CO$, $^{13}CO$, $HCO^+$, and CS have been recently detected with high sensitivity (i.e., main-beam rms noise of tens of mK) with the 13.7 m millimeter telescope of the Purple Mountain Observatory in Delingha by Liu et al. (2021). In one of the nine regions, i.e., G176.51+00.20, a neutral stellar

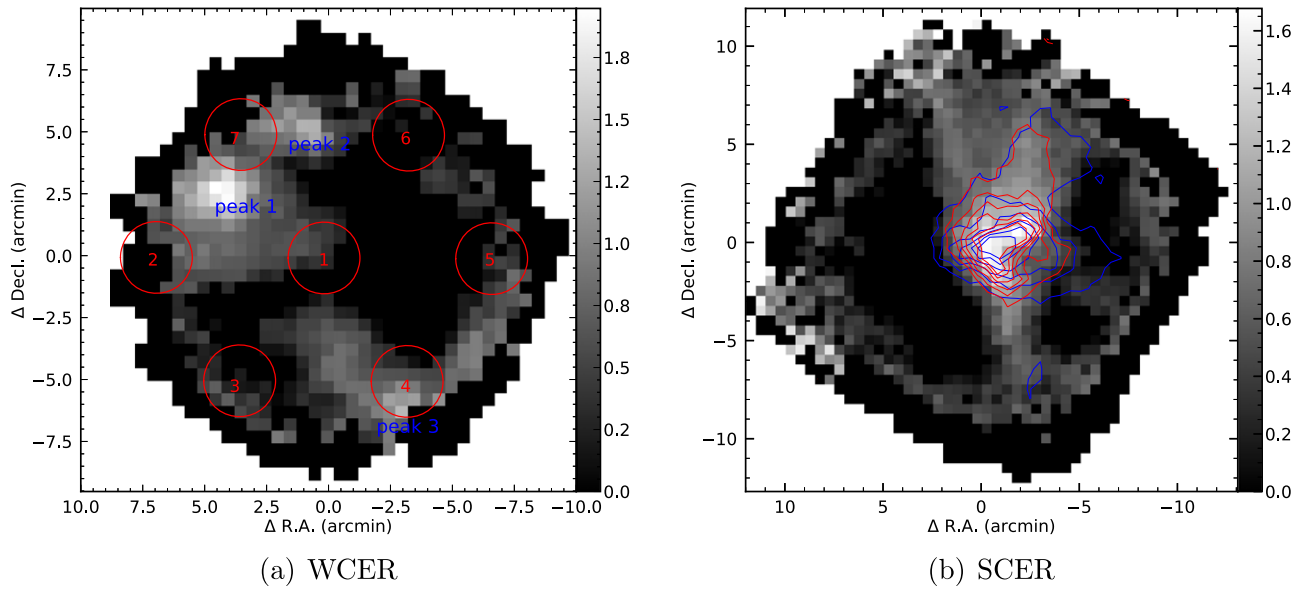(a) WCER                                                    (b) SCER

**Figure 1.** Integrated intensity map of WCER (left) and SCER (right). Left: the background map is the integrated intensity map of $^{12}$CO in the range of $[-5, -1]$ km s$^{-1}$. Peaks 1–3 label the peaks in the WCER (i.e., corresponding to the intensity peaks in the $^{12}$CO map), and the red circles and numbers present the positions and indices of the central seven beams of FAST. Right: the background is an integrated intensity map of C$^{18}$O in the range of $[-30, -10]$ km s$^{-1}$, where the blue and red contours show the integrated intensity map of $^{12}$CO and $^{13}$CO in the same velocity range as the C$^{18}$O map, respectively. Their levels are 0.3, 0.4, 0.5, 0.6, 0.7, and 0.8 times the corresponding peak intensity. The color bars in the left and right panels are in units of (K km s$^{-1}$)$^{1/2}$.

wind traced by atomic hydrogen (H I wind) has also been detected (Li et al. 2022). Therefore, studying HINSA toward G176.51 +00.20 not only would be a bridge to connect the atomic and molecular gas therein, but may also be helpful for studying the relationship between H I winds and molecular outflows.

G176.51+00.20, an active high-mass star-forming region, is located 1.8 kpc from Earth (Moffat et al. 1979; Snell et al. 1988). The dense NH$_3$ core in the center of this region has become synonymous with this region (e.g., Torrelles et al. 1992a; Chen et al. 2003; Jiang et al. 2013). The central engine of this massive star-forming region was identified as a zero-age main-sequence B3 star by using a 3.6 cm map produced from Very Large Array observations (Torrelles et al. 1992b). A more detailed description of this region was provided by Dewangan (2019), where the center of the region of study in this work was marked "H II region" in their Figure 1(a).

The remainder of this paper is organized as follows. In Section 2, we describe the data used in this work. Section 3 presents the results of the HINSA survey toward G176.51 +00.20 and the physical properties of the HINSA features and those of the corresponding molecular lines. In Section 4, we discuss the association between the HINSA features and the molecular clouds, estimate the abundance of the HINSA features, and summarize our results.

## 2. Data

### 2.1. H I Observations with FAST

The most sensitive ground-based single-dish radio telescope is the Five-hundred-meter Aperture Spherical radio Telescope,[6] which is located in Guizhou Province of southwest China (Nan 2006; Nan et al. 2011; Qian et al. 2020). By using the 19-beam receiver that FAST is equipped with (see Li et al. 2018; Jiang et al. 2019, 2020), we observed highly sensitive and high-velocity-resolution H I spectra toward G176.51+00.20. The

mean main-beam rms noise for the 19 obtained spectra is $\sim$7 mK @ 0.1 km s$^{-1}$ resolution. The observations were conducted on 2021 August 19 and 20, with a total integration time of 335 minutes. The HPBW is $\sim$2.9′ at 1.4 GHz, and the pointing error is $\sim$0.′2 (see Jiang et al. 2019, 2020).

### 2.2. Summary of Molecular Lines Observed toward G176.51+00.20

Five high-sensitivity molecular lines were observed toward G176.51+00.20 (with a cell of $\sim$15′ × 15′) by using the 13.7 m telescope: $^{12}$CO ($J = 1-0$) (115.271 GHz), $^{13}$CO ($J = 1-0$) (110.201 GHz), and C$^{18}$O ($J = 1-0$) (109.782 GHz) observed from 2019 July to November; HCO$^+$ ($J = 1-0$) (89.189 GHz) observed from 2019 November to 2020 February; and CS ($J = 2-1$) (97.981 GHz) observed in 2020 May (for more details, see Tables 2–3 of Liu et al. 2021). The velocity resolution of these lines ranges from 0.159 to 0.212 km s$^{-1}$ (the corresponding channel width is 61 kHz), and the HPBW ranges from 49″ to 61″. The lines were observed with the on-the-fly mode and gridded to 30″ pixels. The rms noises range from $\sim$60.9 to $\sim$15.3 mK (for more details, see Liu et al. 2021).

## 3. Data Analysis and Results

Because the molecular-line observations are confined to the central $\sim$15′ × 15′ region centered at (R.A., Decl.) (J2000) = (05$^h$37$^m$52$^s$1, 32°00′03″0), the HINSA survey is also limited to the corresponding regions; i.e., central seven beams (beams 1–7; see Figure 1(a)). We followed the method of Liu et al. (2022) to extract HINSA features. To extract HINSA, it was required to understand the physical properties of the emission regions, at least the central velocity, $v_{c,m}$, velocity dispersion, $\sigma_m$, and excitation temperature, $T_{ex}$ (i.e., the initial conditions to extract HINSA; see Liu et al. 2022). These three physical parameters were obtained by using the high-sensitivity molecular-line observations of the high-mass star-forming region G176.51+00.20 made by Liu et al. (2021).
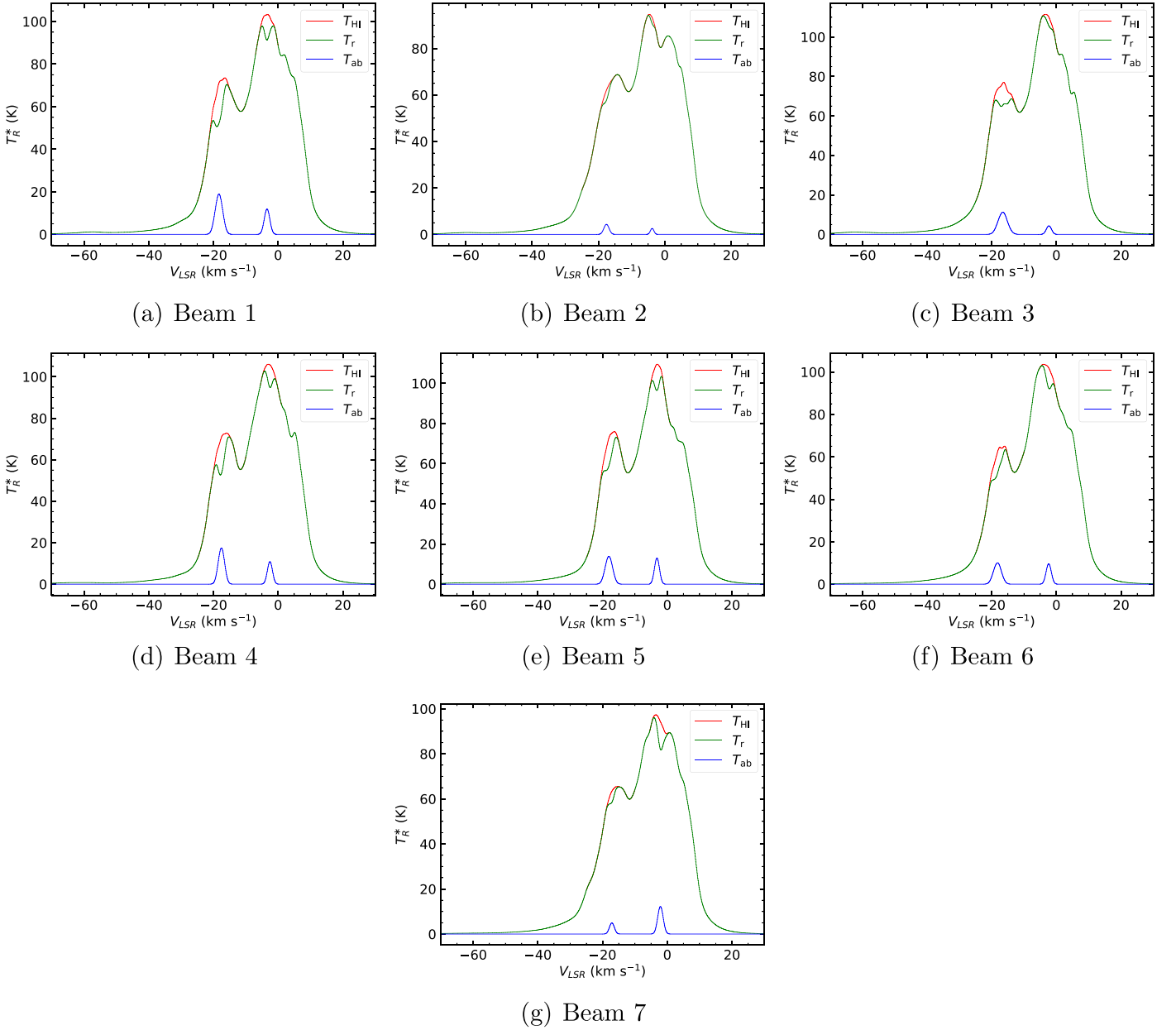
---

(a) Beam 1

(b) Beam 2

(c) Beam 3

(d) Beam 4

(e) Beam 5

(f) Beam 6

(g) Beam 7

**Figure 2.** HINSA features of Beams 1–7, where the green lines (marked as $T_r$) show the observed spectrum, the red lines (marked as $T_{HI}$) the recovered spectrum of H I, and the blue lines (marked as $T_{ab}$) the fitted spectrum of the HINSA features.

## 3.1. Overview of the Region with High-sensitivity Molecular-line Observations

From the study of molecular outflows toward G176.51+00.20 by Liu et al. (2021), the velocity of the most conspicuous components is $\sim-18\,\mathrm{km\,s^{-1}}$, which corresponds to a high-mass star-forming region with a strong bipolar outflow (see Snell et al. 1988; Zhang et al. 2005; Liu et al. 2021). In fact, there is also a weak component with a velocity of $\sim-3\,\mathrm{km\,s^{-1}}$ in the region close to the edge of the observed region. Throughout this work, we have divided the observed region into two parts: a strong CO emission region (hereafter SCER) with a velocity of $\sim-18\,\mathrm{km\,s^{-1}}$ and a weak CO emission region (WCER) with a velocity of $\sim-3\,\mathrm{km\,s^{-1}}$.

Figure 1 presents an integrated intensity map of the WCER (left) and the SCER (right). In the WCER, the $^{13}$CO emission is weak and no C$^{18}$O emission is detected. Therefore, only the

integrated intensity map of $^{12}$CO, with a velocity range of $[-5, -1]\,\mathrm{km\,s^{-1}}$, is presented here. There are three peaks in the CO map of the WCER; i.e., Peaks 1–3 (see the labels in Figure 1(a)). In the SCER, there is strong $^{12}$CO (blue contours), $^{13}$CO (red contours), and C$^{18}$O (background map) emission, where the velocity range of the maps is $[-30, -10]\,\mathrm{km\,s^{-1}}$. Because the various emission components are all connected, and it is difficult to distinguish each of them clearly, we marked the position centered at the peak intensity of C$^{18}$O as Peak 4. We note that this large emission region covers, in fact, almost the entire observed region (including the regions covered by all seven FAST beams; see below).

In the WCER, because the line emission of $^{13}$CO is weak and lines from other molecules (i.e., C$^{18}$O, HCO$^+$, and CS) are not detected, we only conducted Gaussian fits for the $^{12}$CO spectra. The values of $v_{c,m}$ and $\sigma_m$ are given based on those Gaussian fits. The peak brightness temperatures of the $^{12}$CO

**Table 1**
Physical Parameters of the HINSA Features

| Beams | Index | $V_{\mathrm{LSR}}$ (km s$^{-1}$) | $\sigma_{\mathrm{HI}}$ (km s$^{-1}$) | $\tau_{\mathrm{HI}}$ | $T_{\mathrm{ex}}$ (K) | $T_{\mathrm{ab}}$ (K) | $N_{\mathrm{HI}}$ (10$^{18}$ cm$^{-2}$) |
|---|---|---|---|---|---|---|---|
| (1) | (2) | (3) | (4) | (5) | (6) | (7) | (8) |
| Beam 1 | 1 | $-18.42 \pm 0.02$ | $1.14 \pm 0.02$ | $0.31 \pm 0.01$ | $20.30 \pm 0.08$ | $18.97 \pm 0.008$ | $33.1 \pm 1.1$ |
| | 2 | $-3.47 \pm 0.02$ | $0.85 \pm 0.02$ | $0.12 \pm 0.01$ | $7.18 \pm 0.18$ | $11.89 \pm 0.008$ | $3.4 \pm 0.3$ |
| Beam 2 | 1 | $-17.65 \pm 0.02$ | $0.78 \pm 0.02$ | $0.07 \pm 0.01$ | $20.30 \pm 0.08$ | $4.33 \pm 0.006$ | $5.3 \pm 0.7$ |
| | 2 | $-3.83 \pm 0.02$ | $0.53 \pm 0.02$ | $0.03 \pm 0.01$ | $7.18 \pm 0.18$ | $2.57 \pm 0.006$ | $0.5 \pm 0.2$ |
| Beam 3 | 1 | $-16.65 \pm 0.02$ | $1.46 \pm 0.02$ | $0.16 \pm 0.01$ | $20.30 \pm 0.08$ | $11.25 \pm 0.007$ | $21.5 \pm 1.4$ |
| | 2 | $-2.35 \pm 0.09$ | $0.80 \pm 0.09$ | $0.04 \pm 0.01$ | $5.08 \pm 0.31$ | $4.36 \pm 0.007$ | $0.8 \pm 0.2$ |
| Beam 4 | 1 | $-17.63 \pm 0.02$ | $0.96 \pm 0.02$ | $0.28 \pm 0.01$ | $20.30 \pm 0.08$ | $17.47 \pm 0.011$ | $25.4 \pm 0.9$ |
| | 2 | $-2.57 \pm 0.09$ | $0.78 \pm 0.09$ | $0.11 \pm 0.01$ | $5.08 \pm 0.31$ | $10.88 \pm 0.011$ | $2.0 \pm 0.2$ |
| Beam 5 | 1 | $-18.19 \pm 0.02$ | $1.15 \pm 0.02$ | $0.21 \pm 0.01$ | $20.30 \pm 0.08$ | $13.91 \pm 0.006$ | $22.8 \pm 1.1$ |
| | 2 | $-3.23 \pm 0.09$ | $0.77 \pm 0.09$ | $0.13 \pm 0.01$ | $5.08 \pm 0.31$ | $13.01 \pm 0.006$ | $2.3 \pm 0.3$ |
| Beam 6 | 1 | $-18.38 \pm 0.02$ | $1.24 \pm 0.02$ | $0.18 \pm 0.01$ | $20.30 \pm 0.08$ | $10.06 \pm 0.006$ | $20.5 \pm 1.2$ |
| | 2 | $-2.41 \pm 0.02$ | $0.80 \pm 0.02$ | $0.10 \pm 0.01$ | $4.76 \pm 0.16$ | $9.61 \pm 0.006$ | $1.7 \pm 0.2$ |
| Beam 7 | 1 | $-17.19 \pm 0.02$ | $0.76 \pm 0.02$ | $0.08 \pm 0.01$ | $20.30 \pm 0.08$ | $4.94 \pm 0.008$ | $5.7 \pm 0.7$ |
| | 2 | $-2.14 \pm 0.02$ | $0.83 \pm 0.02$ | $0.14 \pm 0.01$ | $4.76 \pm 0.16$ | $12.23 \pm 0.008$ | $2.5 \pm 0.2$ |

**Note.** Columns 3–8 present the central velocity, velocity dispersion, optical depth, excitation temperature, peak intensity, and column density of HINSA features.

spectra, $T_{\mathrm{peak}}^{12\mathrm{CO}}$, were used to calculate the value of $T_{\mathrm{ex}}$ (e.g., Garden et al. 1991) as

$$T_{\mathrm{ex}} = \frac{5.53}{\ln\left(1 + \frac{5.53}{T_{\mathrm{peak}}^{12\mathrm{CO}} + 0.82}\right)}. \qquad (1)$$

The results of $v_{\mathrm{c,m}}$, $\sigma_{\mathrm{m}}$, and $T_{\mathrm{ex}}$, with $1\sigma$ errors, are $-3.92 \pm 0.01$, $0.35 \pm 0.01$ km s$^{-1}$, and $7.18 \pm 0.18$ K for Peak 1, and $-2.20 \pm 0.01$, $0.44 \pm 0.01$ km s$^{-1}$, and $4.76 \pm 0.16$ K for Peak 2, and $-2.54 \pm 0.04$, $0.42 \pm 0.04$ km s$^{-1}$, and $5.08 \pm 0.31$ K for Peak 3, respectively. In the SCER, the value of $T_{\mathrm{ex}}$ was also calculated based on $T_{\mathrm{peak}}^{12\mathrm{CO}}$. The values of $v_{\mathrm{c,m}}$ and $\sigma_{\mathrm{m}}$ are based on the Gaussian fit of the $^{13}$CO spectrum. The values of $v_{\mathrm{c,m}}$, $\sigma_{\mathrm{m}}$, and $T_{\mathrm{ex}}$ are $-18.53 \pm 0.01$, $1.13 \pm 0.01$ km s$^{-1}$, and $20.30 \pm 0.08$ K, respectively. These values were used to extract the HINSA features.

### 3.2. HINSA Features

To extract as many HINSA features as possible, we assumed that, for the spectrum of each FAST beam, HINSA features corresponding to each of the four components of the molecular clouds (i.e., Peaks 1–4) exist. The specific description of the method used to extract the HINSA feature is presented in Section A.

We extracted 14 HINSA features in total from the seven beams (see Figure 2). Their velocity, $V_{\mathrm{LSR}}$, peak intensity, $T_{\mathrm{ab}}$, optical depth, $\tau_0$, and velocity dispersion, $\sigma_{\mathrm{HI}}$, with $1\sigma$ errors are listed in Table 1.

The fitted values of $\tau_0$ and $\sigma_{\mathrm{HI}}$ were used to calculate the column density of the HINSA features, $N_{\mathrm{HI}}$ (see Li & Goldsmith 2003), as

$$N_{\mathrm{HI}} = 1.95 \times 10^{18} \tau_0 T_{\mathrm{ex}} \Delta V, \qquad (2)$$

where $\Delta V = \sqrt{8\ln(2)}\,\sigma_{\mathrm{HI}}$. The results of $N_{\mathrm{HI}}$ and the corresponding $T_{\mathrm{ex}}$ with $1\sigma$ errors are listed in Table 1. The values of $N_{\mathrm{HI}}$ range from $\sim 5.3$ to $33.1 \times 10^{18}$ cm$^{-2}$ in the SCER and from $\sim 0.5$ to $3.4 \times 10^{18}$ cm$^{-2}$ in the WCER.

### 3.3. Physical Properties of the Molecular-line Emission

To make a comparison between the HINSA features and the molecular-line emission, we resampled the molecular data observed by Liu et al. (2021) to pixel sizes of $3' \times 3'$ and aligned the pixel center of molecular emission with the corresponding FAST beam center.

Figure 3 presents the molecular-line emission, corresponding to each beam as well as the corresponding HINSA features, i.e., $T_{\mathrm{ab}}$, after resampling. $^{12}$CO emission with a velocity of $\sim -18$ km s$^{-1}$ (i.e., the SCER) is detected in all seven beams, indicating that the detected $^{12}$CO emission in the SCER covers almost the entire observed region of the molecular lines. The line centers and velocity dispersions of the molecular lines are from the Gaussian fits to the $^{12}$CO, $^{13}$CO, and/or C$^{18}$O spectra. We also calculated the column density of all observed molecular species, i.e., $^{12}$CO, $^{13}$CO, C$^{18}$O, HCO$^+$, and CS when these were detected (see Section B). The velocity center, velocity dispersion, and column density, as well as the corresponding $T_{\mathrm{ex}}$, are listed in Table B1.

## 4. Discussion and Conclusions

### 4.1. Association between the HINSA Features and the Molecular Clouds

The association between the HINSA features and the molecular-line emissions can be seen in Figure 3. In the SCER (shown as the first entry for each beam in Table 1), the HINSA features are probably associated with the molecular-line emission. In the WCER (shown as the second entry in Table 1), no molecular-line emission associated with HINSA features is detected toward Beams 1, 3, 4, and 6. The only detected $^{12}$CO emission, corresponding to Beams 2, 5, and 7, is also weak. The HINSA features in the WCER are probably associated with CO-dark or CO-faint gas (e.g., Wolfire et al. 2010; Tang et al. 2016; Liu et al. 2022). This is an issue worthy of further observations.

In addition, a further quantitative comparison was conducted regarding the relationship between the center velocity and the nonthermal velocity dispersion of the HINSA features and the molecular gases. In the SCER, the differences between the center
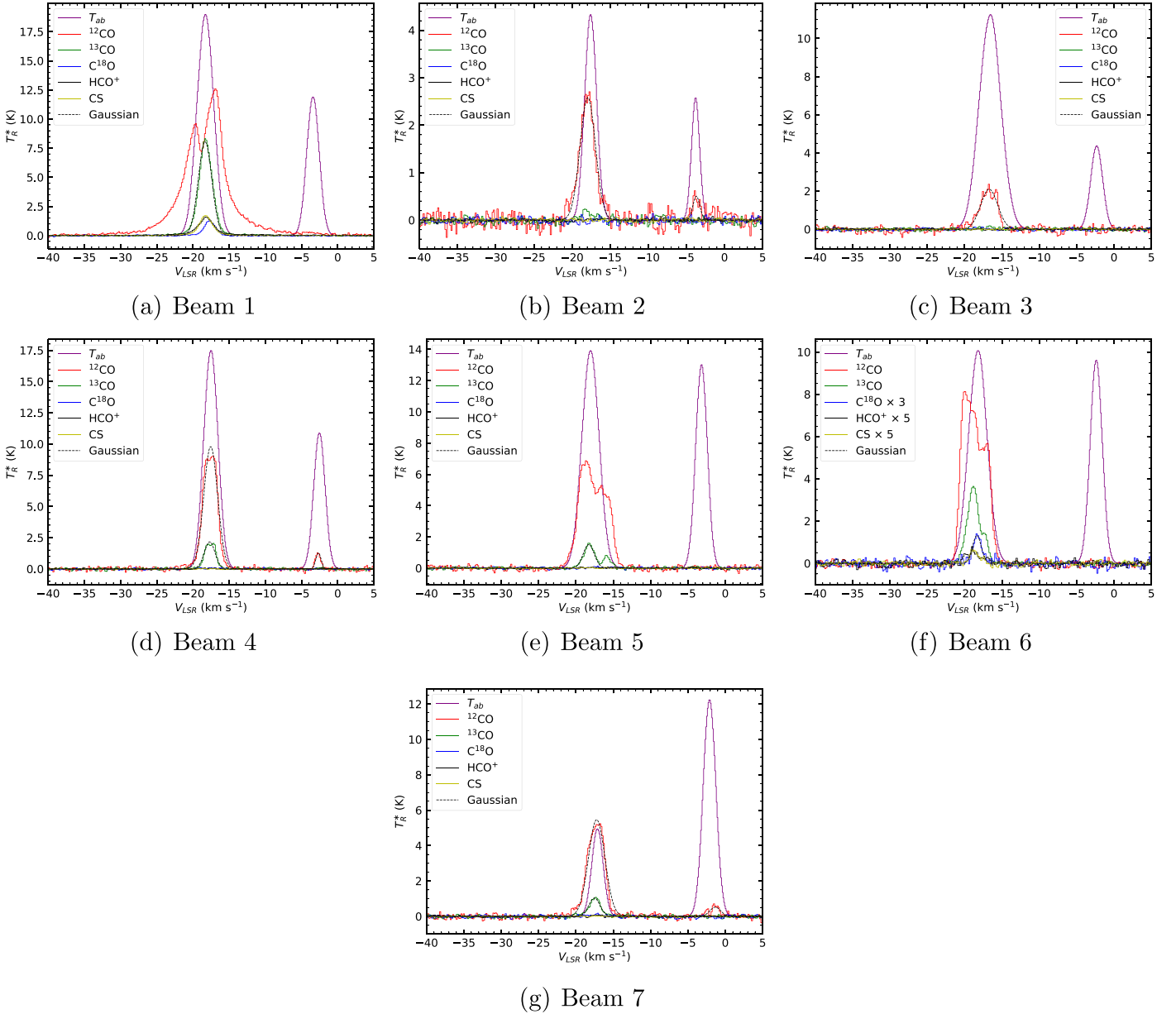
**Figure 3.** HINSA features in Beams 1–7 and the molecular-line spectra of the corresponding regions. The red, green, blue, black, and yellow lines show the spectra of $^{12}CO$, $^{13}CO$, $C^{18}O$, $HCO^+$, and CS, respectively, and the purple lines represent the HINSA features. We fitted the profiles of both $^{12}CO$ and $^{13}CO$ with a Gaussian profile for each component, except for spectra that showed strong self-absorption or were contaminated by other components. For Beam 6, only the line emission of $C^{18}O$ was fitted because there was strong self-absorption in the spectra of $^{12}CO$ and $^{13}CO$.

velocity of the HINSA features (see Table 1) and those of the $^{12}CO$, $^{13}CO$, and/or $C^{18}O$ lines are within the velocity resolution of the CO spectra (i.e., $\sim 0.2\,km\,s^{-1}$). This indicates that the HINSA features are associated with the molecular clouds traced by the CO. The nonthermal velocity dispersion of the HINSA features, $\sigma_{nt,HI} = \sqrt{\sigma_{HI}^2 - kT_{ex}/m_H}$, is smaller than that of the $^{12}CO$ lines, $\sigma_{nt,^{12}CO} = \sqrt{\sigma_{^{12}CO}^2 - kT_{ex}/m_{^{12}CO}}$, and is similar to that of the $^{13}CO$ lines, $\sigma_{nt,^{13}CO} = \sqrt{\sigma_{^{13}CO}^2 - kT_{ex}/m_{^{13}CO}}$, except for that in Beam 3, where the value of $\sigma_{nt,HI}$ is larger than that of $\sigma_{nt,^{12}CO}$ by $\sim 20\%$ (see $\sigma_{HI}$ in Table 1 and $\sigma_{^{12}CO}$ and $\sigma_{^{13}CO}$ in Table B1). This result is in agreement with that of Li & Goldsmith (2003), indicating that the HINSA in the SCER is probably mixed with the gas in cold and well-shielded regions of the molecular clouds.

In the WCER, the association between the HINSA features and the CO cloud appears to be poor. First, the difference between the center velocity of the HINSA features (see Table 1) and that of $^{12}CO$ is larger than in the case of the SCER, and the maximum difference reaches $\sim 0.8\,km\,s^{-1}$ (i.e., in Beam 7). Second, the value of $\sigma_{nt,HI}$ is larger than that of $\sigma_{nt,^{12}CO}$. No $^{13}CO$ emission is detected toward the regions corresponding to all seven beams after resampling. In fact, we also do not detect any $^{13}CO$ emission in Beam 3 in the SCER, and the value of $\sigma_{nt,HI}$ in this region is larger than that of $\sigma_{nt,^{12}CO}$. Therefore, it is probably more accurate to classify Beam 3 in the SCER as a WCER component. The discussion below is based on this reclassification. We also find that the value of $\sigma_{HI}$ in the WCER (including Beam 3 in the SCER) is comparable to some of the values found by Tang et al. (2016) for CO-dark clouds. These facts indicate that the HINSA
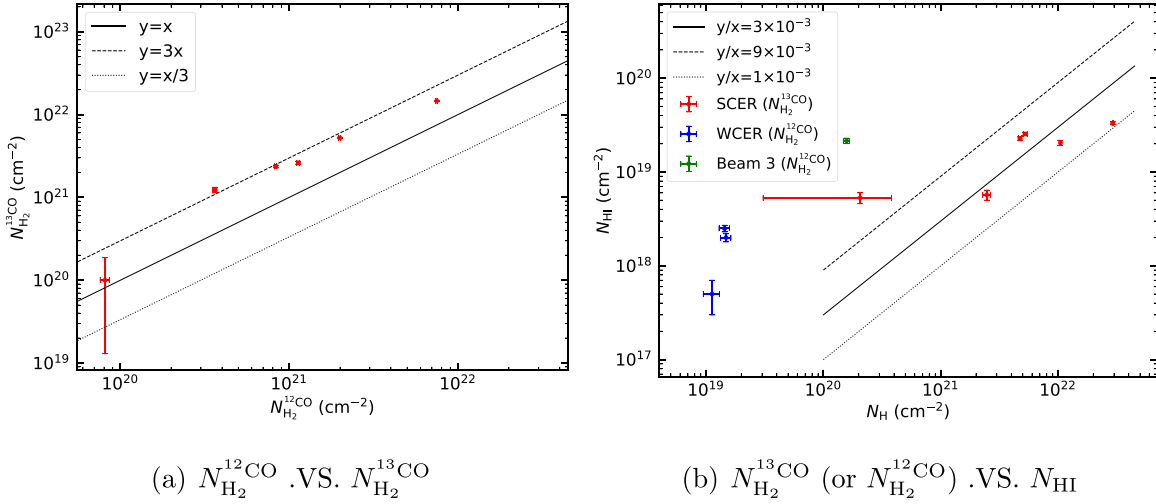
THE ASTROPHYSICAL JOURNAL LETTERS, 933:L26 (11pp), 2022 July 10

Li et al.





(a) $N_{H_2}^{12CO}$ .VS. $N_{H_2}^{13CO}$

(b) $N_{H_2}^{13CO}$ (or $N_{H_2}^{12CO}$) .VS. $N_{HI}$

**Figure 4.** Left: comparison of $N_{H_2}^{12CO}$ and $N_{H_2}^{13CO}$ in the SCER, where $^{13}$CO is not detected in Beam 3. Right: comparison of the column density of HINSA, $N_{HI}$, and of the total gas, $N_H$. The red points represent the results corresponding to the SCER (except for Beam 3), where the column density of the molecular clouds is traced by $^{13}$CO. The blue points present the results corresponding to the WCER, where the column density of the molecular clouds is traced by $^{12}$CO. The green points indicate the result corresponding to Beam 3 in the SCER (which may be more suitably classified as a WCER component), where the column density of the molecular clouds is traced by $^{12}$CO.

toward the WCER is probably not mixed with CO clouds but probably associated with more diffuse CO-dark or CO-faint clouds. Further observations of C I, C II, and/or OH may be helpful in clarifying the relationship between the HINSA features and the CO-dark or CO-faint gas (e.g., Li & Goldsmith 2003; Wolfire et al. 2010; Tang et al. 2016) toward the WCER.

### 4.2. Abundance of H I the HINSA Features

The fractional abundance of HINSA, $X_{HI}$, based on the column density is valuable. In this case, $X_{HI} = N_{HI}/N_H$, where $N_{HI}$ is the column density of the HINSA, and $N_H = N_{HI} + 2N_{H_2}$. $N_{H_2}$ is the column density of H$_2$ in the molecular cloud, which can be traced by $^{12}$CO, $^{13}$CO, C$^{18}$O, HCO$^+$, and CS, i.e., $N_{H_2}^{12CO}$, $N_{H_2}^{13CO}$, $N_{H_2}^{C18O}$, $N_{H_2}^{HCO^+}$, and $N_{H_2}^{CS}$ (see Table B1).

We compared the values of $N_{H_2}^{12CO}$ and $N_{H_2}^{13CO}$ within all regions where we simultaneously detected $^{12}$CO and $^{13}$CO line emission (i.e., Beams 1, 2, and 4–7 of the SCER). The results show that the value of $N_{H_2}^{13CO}$ is larger than that of $N_{H_2}^{12CO}$ by a factor of $\lesssim 3$, indicating that $N_{H_2}^{13CO}$ is a better indicator of the column density of the molecular clouds. The values of $N_{H_2}^{12CO}$ are probably underestimated due to optical depth effects on the $^{12}$CO spectra. In addition, the species tracing higher densities, i.e., C$^{18}$O, HCO$^+$, and CS, are detected only in Beams 1 and 6. In Beam 1, the ratios of the column density traced by $^{13}$CO, $N_{H_2}^{13CO}$, to those traced by the three dense gas tracers, $N_{H_2}^{C18O}$, $N_{H_2}^{HCO^+}$, and $N_{H_2}^{CS}$, are $\sim 0.92$, $\sim 1.48$, and $\sim 0.78$, respectively, indicating that $N_{H_2}^{13CO}$ is a good measure of the column density of the molecular cloud. In Beam 6, the dilution of the dense gas tracers is relatively stronger (see Figure 1(b)). Nevertheless, $N_{H_2}^{13CO}/N_{H_2}^{C18O} \sim 1.2$ also indicates that $^{13}$CO is a good tracer of the molecular cloud. Therefore, we used $N_{H_2}^{13CO}$ to represent the column density of molecular clouds in the SCER.

The abundance of HINSA, $X_{HI}$, in most cases of the SCER (i.e., Beams 1 and 4–7) ranges from $\sim 1.1 \times 10^{-3}$ to $\sim 4.8 \times 10^{-3}$ (see the red points in Figure 4(b)). The one exception is the value of $X_{HI}$ is $\sim 2.6 \times 10^{-2}$ in Beam 2, where the value of $N_{H_2}^{13CO}$ is one

order of magnitude smaller than those in the other five beams (i.e., Beams 1 and 4–7), and the relative error of $N_{H_2}^{13CO}$ is large (see Figure 4(b) and Table B1). The abundances of HINSA in Beams 1 and 4–7 are similar to those toward optically selected dark clouds and molecular cores (i.e., with an average value of $\sim 1.5 \times 10^{-3}$; Li & Goldsmith 2003; Krčo & Goldsmith 2010). The HINSA abundances in the SCER (including Beam 2) fall into the HINSA abundance range toward the PGCC sources (i.e., from $5.1 \times 10^{-4}$ to $1.3 \times 10^{-2}$) of Tang et al. (2020), but larger than the HINSA abundances derived from other PGCC sources (i.e., $\sim 3 \times 10^{-4}$ varied by a factor of $\sim 3$) by Liu et al. (2022).

The HINSA abundance toward Beam 1 is consistent with the abundance of H I in the H I wind (i.e., the ratio of the column density of the H I wind to that of the total outflowing gas) in the same beam. This fact indicates that HINSA is probably a physical bridge that connects H I winds and molecular outflows.

We also find that the value of $X_{HI}$ in Beam 1 is smaller than the values obtained from the surrounding beams (i.e., Beams 2–7; see Figure 1(a)). This structure seems to be a ring, but unlike that observed by Zuo et al. (2018), the abundance of HINSA, $X_{HI}$, diminishes toward the center of the cloud. One of the reasons for this could be that the central high-mass zero-age main-sequence B3 star (see Torrelles et al. 1992a) ionizes the H I detected in Beam 1 in the SCER, which is located in a H II region (see Dewangan 2019). This then decreases the abundance of H I. The ionization can be studied using radio recombination lines (e.g., Zhang et al. 2014, 2021).

The mean densities of H I, $\bar{n}_{HI}$, and total proton, $\bar{n}_H$, in Beam 1 are $\sim 7.2$ and $\sim 6.1 \times 10^3$ cm$^{-3}$, respectively, assuming that the cloud diameter is $\sim 1.5$ pc, corresponding to the diameter of FAST being the HPBW. We assume that the density profile has a constant-density core surrounded by an envelope of the form

$$n(r) = \frac{2n_0}{1 + (r/r_0)^2}, \qquad (3)$$

where $n_0$ and $r_0$ (set to $10^{17}$ cm) are the central density and the radius of the constant-density core. In this case, $n_0 \sim 9.4 \, \bar{n}_H$ would be larger than that of model 1 in Goldsmith et al. (2007), indicating that the density is high enough to initiate the

conversion of H I → H₂. Following the model developed by Goldsmith et al. (2007), the time that has elapsed since the material was UV irradiated is $\sim 2 \times 10^5$ yr (see Appendix C), during which H I could convert to H₂. This time is consistent with the timescale of the star formation in this region (i.e., $\sim 2 \times 10^5$ yr) derived from near-infrared H₂ knots by Chen et al. (2003). The model of Goldsmith et al. (2007) also implies another possible reason why $X_{HI}$ diminishes toward the center of the cloud, i.e., the conversion to molecular form occurs more rapidly in the higher-density inner region.

In the WCER, a comparison of $N_{HI}$ and $N_H$ (only for the regions where CO emission is detected) is plotted as blue and green points in Figure 4(b). The abundance of the HINSA features, $X_{HI}$, is $\sim 0.04$, $\sim 0.14$, and $\sim 0.17$ in Beams 2, 4, and 7, respectively. The value of $X_{HI}$ is $\sim 0.14$ in Beam 3 in the SCER where ¹³CO emission is not detected. The high abundances are most likely caused by an underestimation of the column density of the molecular clouds because the associated molecular clouds (including the region in Beam 3 in the SCER) are probably CO-dark or CO-faint gas (e.g., Bolatto et al. 2013; Tang et al. 2016).

The comparison of the HINSA features and the molecular-line emission indicates that the HINSA is probably mixed with the gas in cold and well-shielded CO clouds in which ¹³CO emission is detected. There are HINSA features that have no detected ¹³CO and/or ¹²CO emission counterparts, meaning they are probably associated with CO-dark or CO-faint gas. In addition, HINSA is a promising physical bridge that connects the H I winds with molecular outflows. There is a possible ring where the abundance of HINSA diminishes toward the center of the cloud.

## Appendix A
## Extracting HINSA

The method used here to extract HINSA is based on the methodology developed by Liu et al. (2022). The first step of this method is to obtain the initial values of the optical depth, $\tau_i$, velocity dispersion, $\sigma_i$, and central velocity, $v_i$. $\tau_i$ is initially set to 0.1. Obtaining the initial values of $v_i$ and $\sigma_i$ requires knowledge derived from the corresponding high-sensitivity CO spectrum, including the central velocity, $v_{c,m}$, velocity dispersion, $\sigma_m$, and excitation temperature, $T_{ex}$. To extract as much HINSA as possible, we assume that every component of CO emission (i.e., Peaks 1–4) corresponds to a HINSA feature. The

initial value of $v_i$ equals $v_{c,m}$, and the initial value of $\sigma_i$ reads as

$$\sigma_i = \sqrt{\sigma_m^2 + \frac{kT_{ex}}{m_H} - \frac{kT_{ex}}{m_{CO}}}, \quad (A1)$$

where $k$ is the Boltzmann constant, $m_H$ the mass of atomic hydrogen, and $m_{CO}$ the mass of the ¹²CO molecule for Peaks 1–3 and of the ¹³CO molecule for Peak 4.

The optical depth of a HINSA feature can be written (Krčo et al. 2008) as

$$\tau(v) = \sum_{m-1}^{i=0} \tau_i e^{-\frac{(v-v_i)^2}{2\sigma_i^2}}, \quad (A2)$$

where $\tau_i$, $\sigma_i$, and $v_i$ are the initial values of the optical depth, velocity dispersion, and central velocity of the $i$th component of the HINSA features, respectively.

H I emission free of self-absorption, $T_{HI}$, and the self-absorption of H I, $T_{ab}$, satisfies (Li & Goldsmith 2003)

$$T_{ab} = T_{HI} - T_r = [pT_{HI} + (T_c - T_{ex})(1 - \tau_f)](1 - e^{-\tau}), \quad (A3)$$

where $p$ is a parameter representing the proportion of the background H I optical depth, $T_r$ is the observed H I spectrum, $T_c$ is the H I continuum brightness temperature, $T_{ex}$ is the excitation temperature (derived from the spectrum of ¹²CO), and $\tau_f$ is the foreground H I optical depth.

Following the treatment of Liu et al. (2022), $p$ was set to unity, and then $\tau_f = 0$. $T_{ex}$ and $T_c$ were simultaneously ignored. $T_{HI}$ then can be expressed as

$$T_{HI} = T_r e^\tau, \quad (A4)$$

which can be rewritten as

$$T_{HI} = T_r + (1 - e^\tau)T_{HI,smooth}^f, \quad (A5)$$

where $T_{HI,smooth}^f$ is the polynomial fit of $T_{HI}$.

$\tau_i$, $\sigma_i$, and $v_i$ (Krčo et al. 2008) could be obtained by minimizing $\mathcal{R}$ as

$$\mathcal{R} \cong \sum_{j=1}^N (T''_{HI})_j^2 \Delta_{ch}, \quad (A6)$$

where

$$T''_{HI} = \frac{T_{HI,j+1} + T_{HI,j-1} - 2T_{HI,j}}{\Delta_{ch}^2}, \quad (A7)$$

and where $\Delta_{ch}$ is the channel width of the H I spectrum and $j$ the index of the channel. Similar to Liu et al. (2022), the L-BFGS-B algorithm from Scipy[7] (Virtanen et al. 2020) was used to obtain $\tau_i$, $\sigma_i$, and $v_i$. For more details on the methodology of extracting HINSA, see Liu et al. (2022). The final values of the optical depth, velocity dispersion, and central velocity of the HINSA features are denoted $\tau_0$, $\sigma_{HI}$, and $V_{LSR}$, respectively.

---

[7] https://www.scipy.org/

## Appendix B
## Column Densities of the Molecules

For the tracer of $^{13}CO$, under local thermal equilibrium, the column density of $H_2$, $N_{H_2}^{13CO}$, is (Snell et al. 1984)

$$N_{H_2}^{13CO} = 2.3 \times 10^{19} \frac{T_{ex}}{e^{-5.29/T_{ex}}}$$
$$\times \int \frac{e^{\tau_{13CO}}}{1 - e^{-\tau_{13CO}}} T_{mb}^{13CO} dv, \quad (B1)$$

where $X_{13CO} = [^{13}CO]/[H_2] = 2 \times 10^{-6}$ is used (Dickman 1978). In the third term, the optical depth ($\tau_{13CO}$) correction, $e^{\tau_{13CO}}/(1 - e^{-\tau_{13CO}})$, is considered only when the values of $T_{mb}^{13CO}$ are larger than three times the corresponding rms noise. In this term, the optical depth of $^{13}CO$ is

$$\tau_{13CO} = -\ln\left[1 - \frac{T_{mb}^{13CO}/5.29}{1/(e^{5.29/T_{ex}} - 1) - 0.16}\right]. \quad (B2)$$

$\tau_{13CO}$ can be used to calculate the optical depth of $^{12}CO$, $\tau_{12CO}$, by multiplying the abundance ratio, $[^{12}CO]/[^{13}CO] \sim 50$. The column density of $H_2$ traced by $^{12}CO$ is, therefore,

$$N_{H_2}^{12CO} = 4.2 \times 10^{17} \frac{T_{ex}}{e^{-5.53/T_{ex}}}$$
$$\times \int \frac{e^{\tau_{12CO}}}{1 - e^{-\tau_{12CO}}} T_{mb}^{12CO} dv, \quad (B3)$$

where $X_{12CO} = [^{12}CO]/[H_2] = 10^{-4}$ is used in this work (Snell et al. 1984). If $^{13}CO$ emission is not detected, the optical depth correction in the third term is set to unity.

Similarly, the column density of $H_2$ traced by $C^{18}O$ is

$$N_{H_2}^{C^{18}O} = 2.4 \times 10^{20} \frac{T_{ex}}{e^{-5.27/T_{ex}}}$$
$$\times \int \frac{e^{\tau_{C^{18}O}}}{1 - e^{-\tau_{C^{18}O}}} T_{mb}^{C^{18}O} dv, \quad (B4)$$

with

$$\tau_{C^{18}O} = -\ln\left[1 - \frac{T_{mb}^{C^{18}O}/5.27}{1/(e^{5.27/T_{ex}} - 1) - 0.17}\right], \quad (B5)$$

where $X_{C^{18}O} = [C^{18}O]/[H_2] = 2 \times 10^{-7}$ is used (Garden et al. 1991). For $HCO^+$ (Yang et al. 1991) we have

$$N_{H_2}^{HCO^+} = 1.87 \times 10^{19} \frac{T_{ex}}{1 - e^{-4.28/T_{ex}}}$$
$$\times \int \frac{e^{\tau_{HCO^+}}}{1 - e^{-\tau_{HCO^+}}} T_{mb}^{HCO^+} dv, \quad (B6)$$

with

$$\tau_{HCO^+} = -\ln\left[1 - \frac{T_{mb}^{HCO^+}/4.28}{1/(e^{4.28/T_{ex}} - 1) - 0.26}\right], \quad (B7)$$

where $X_{HCO^+} = [HCO^+]/[H_2] = 10^{-8}$ is used (Turner et al. 1997). Finally, for CS we have (Liu et al. 2021)

$$N_{H_2}^{CS} = 1.89 \times 10^{20} \frac{T_{ex}}{e^{-4.70/T_{ex}}} \int \frac{e^{\tau_{CS}}}{1 - e^{-\tau_{CS}}} T_{mb}^{CS} dv, \quad (B8)$$

with

$$\tau_{CS} = -\ln\left[1 - \frac{T_{mb}^{CS}/4.70}{1/(e^{4.70/T_{ex}} - 1) - 0.22}\right], \quad (B9)$$

where $X_{CS} = [CS]/[H_2] = 10^{-9}$ is used (Tatematsu et al. 1998). $N_{H_2}^{12CO}$, $N_{H_2}^{13CO}$, $N_{H_2}^{C^{18}O}$, $N_{H_2}^{HCO^+}$, and $N_{H_2}^{CS}$ are listed in Table B1.

**Table B1**
Physical Parameters Traced by the Molecules

| Beams | Index | $V_{^{12}CO_1}$ (km s$^{-1}$) | $V_{^{13}CO_1}$ (km s$^{-1}$) | $\sigma_{^{12}CO_1}$ (km s$^{-1}$) | $\sigma_{^{13}CO_1}$ (km s$^{-1}$) | $T_{ex}$ (K) | $N_{H_2}^{^{12}CO}$ (10$^{20}$ cm$^{-2}$) | $N_{H_2}^{^{13}CO}$ (10$^{21}$ cm$^{-2}$) | $N_{H_2}^{C^{18}O}$ (10$^{21}$ cm$^{-2}$) | $N_{H_2}^{HCO^+}$ (10$^{21}$ cm$^{-2}$) | $N_{H_2}^{CS}$ (10$^{21}$ cm$^{-2}$) |
|---|---|---|---|---|---|---|---|---|---|---|---|
| Beam 1 | 1 | ... | $-18.33 \pm 0.04$ | ... | $0.93 \pm 0.04$ | $20.30 \pm 0.08$ | $74.72 \pm 0.73$ | $14.62 \pm 0.08$ | $15.84 \pm 0.53$ | $10.29 \pm 0.13$ | $21.26 \pm 0.16$ |
| Beam 2 | 1 | $-17.93 \pm 0.03$ | ... | $1.01 \pm 0.03$ | ... | $20.30 \pm 0.8$ | $0.81 \pm 0.05$ | $0.10 \pm 0.09$ | ... | ... | ... |
|  | 2 | $-3.69 \pm 0.09$ | ... | $0.45 \pm 0.09$ | ... | $7.18 \pm 0.18$ | $0.05 \pm 0.01$ | ... | ... | ... | ... |
| Beam 3 | 1 | $-16.71 \pm 0.03$ | ... | $1.14 \pm 0.03$ | ... | $20.30 \pm 0.08$ | $0.68 \pm 0.04$ | ... | ... | ... | ... |
| Beam 4 | 1 | $-17.55 \pm 0.01$ | $-17.69 \pm 0.01$ | $0.95 \pm 0.01$ | $0.74 \pm 0.01$ | $20.30 \pm 0.08$ | $11.32 \pm 0.21$ | $2.61 \pm 0.10$ | ... | ... | ... |
|  | 2 | $-2.66 \pm 0.02$ | ... | $0.36 \pm 0.02$ | ... | $5.08 \pm 0.31$ | $0.06 \pm 0.01$ | ... | ... | ... | ... |
| Beam 5 | 1 | ... | $-18.28 \pm 0.02$ | ... | $0.73 \pm 0.04$ | $20.30 \pm 0.08$ | $8.32 \pm 0.14$ | $2.36 \pm 0.08$ | ... | ... | ... |
| Beam 6 | 1 | $-18.35 \pm 0.04$[a] | ... | $0.58 \pm 0.04$[a] | ... | $20.30 \pm 0.08$ | $19.89 \pm 0.27$ | $5.23 \pm 0.09$ | $4.18 \pm 0.90$ | $0.48 \pm 0.14$ | $0.65 \pm 0.23$ |
| Beam 7 | 1 | $-17.22 \pm 0.01$ | $-17.52 \pm 0.02$ | $1.11 \pm 0.01$ | $0.74 \pm 0.02$ | $20.30 \pm 0.08$ | $3.63 \pm 0.10$ | $1.23 \pm 0.09$ | ... | ... | ... |
|  | 2 | $-1.34 \pm 0.09$ | ... | $0.72 \pm 0.09$ | ... | $4.76 \pm 0.16$ | $0.06 \pm 0.01$ | ... | ... | ... | ... |

**Note.**
[a] Determined from the Gaussian fit of the C$^{18}$O spectrum.

## Appendix C
## Transition between Atomic and Molecular Phases

We follow the model developed by Goldsmith et al. (2007) to study the transition between H I and $H_2$. We only focus on the central constant core and assume that the central density is $n_0 \sim 5.7 \times 10^4 \, cm^{-3}$, the line width is $1.14 \, km \, s^{-1}$, the radius is $10^{17}$ cm, and $T = 10$ K. The other parameters follow those in Goldsmith et al. (2007). Equations (3)–(5) in Goldsmith et al. (2007) would produce the evolution of the density of H I, $n_{HI}$, and $H_2$, $n_{H_2}$. Figure 5 shows $n_{HI}$ and $X_{HI}$ as a function of time, where $X_{HI}$ is set to $n_{HI}/(n_{HI} + 2n_{H_2})$ assuming that the sizes of cold H I and CO cloud are similar (see e.g., Goldsmith et al. 2007). The time that has elapsed since the material was UV irradiated would be $\sim 2 \times 10^5$ yr assuming $X_{HI} \sim 1.1 \times 10^{-3}$.
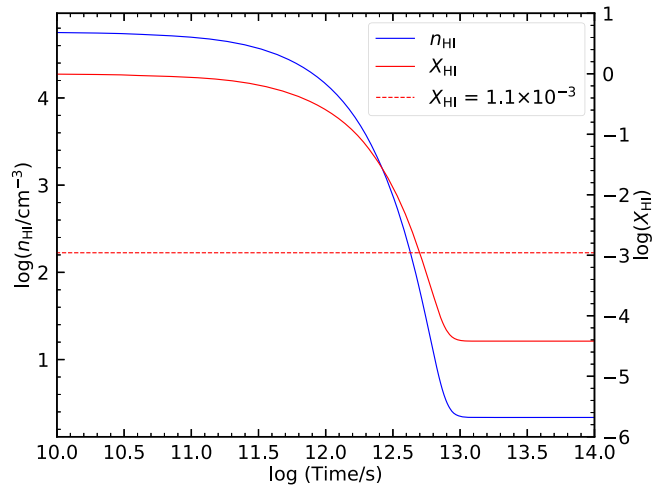


**Figure 5.** $n_{HI}$ and $X_{HI}$ as a function of time. The H I density in the cloud core drops to its steady-state value of $\sim 2 \, cm^{-3}$ with a time of $\sim 4 \times 10^5$ yr.

## ORCID iDs

Yingjie Li https://orcid.org/0000-0001-7526-0120
Ye Xu https://orcid.org/0000-0001-5602-3306
Shuaibo Bian https://orcid.org/0000-0002-7508-9615

## References

Bolatto, A. D., Wolfire, M., & Leroy, A. K. 2013, ARA&A, 51, 207
Chen, Y., Yao, Y., Yang, J., Zeng, Q., & Sato, S. 2003, A&A, 405, 655
Dewangan, L. K. 2019, ApJ, 884, 84
Dickman, R. L. 1978, ApJS, 37, 407
Garden, R. P., Hayashi, M., Gatley, I., Hasegawa, T., & Kaifu, N. 1991, ApJ, 374, 540
Gibson, S. J. 2010, in ASP Conf. Ser. 438, The Dynamic Interstellar Medium: A Celebration of the Canadian Galactic Plane Survey, ed. R. Kothes, T. L. Landecker, & A. G. Willis (San Francisco, CA: ASP)
Gibson, S. J., Taylor, A. R., Higgs, L. A., & Dewdney, P. E. 2000, ApJ, 540, 851
Goldsmith, P. F., & Li, D. 2005, ApJ, 622, 938
Goldsmith, P. F., Li, D., & Krčo, M. 2007, ApJ, 654, 273
Hasegawa, T., Sato, F., & Fukui, Y. 1983, AJ, 88, 658
Heeschen, D. S. 1955, ApJ, 121, 569
Jiang, P., Yue, Y., Gan, H., et al. 2019, SCPMA, 62, 959502
Jiang, P., Tang, N.-Y., Hou, L.-G., et al. 2020, RAA, 20, 064
Jiang, Z.-B., Chen, Z.-W., Wang, Y., et al. 2013, RAA, 13, 695
Knapp, G. R. 1974, AJ, 79, 527
Krčo, M., & Goldsmith, P. F. 2010, ApJ, 724, 1402
Krčo, M., Goldsmith, P. F., Brown, R. L., & Li, D. 2008, ApJ, 689, 276
Lee, C. W., & Myers, P. C. 1999, ApJS, 123, 233
Li, D., & Goldsmith, P. F. 2003, ApJ, 585, 823

Li, D., Wang, P., Qian, L., et al. 2018, IMMag, 19, 112
Li, Y. J., Xu, Y., Xu, J. L., et al. 2022, ApJ, in press
Liu, D.-J., Xu, Y., Li, Y.-J., et al. 2021, ApJS, 253, 15
Liu, X., Wu, Y., Zhang, C., et al. 2022, A&A, 658, A140
Lynds, B. T. 1962, ApJS, 7, 1
Moffat, A. F. J., Fitzgerald, M. P., & Jackson, P. D. 1979, A&AS, 38, 197
Nan, R. 2006, SCPMA, 49, 129
Nan, R., Li, D., Jin, C., et al. 2011, IJMPD, 20, 989
Planck Collaboration, Ade, P. A. R., Aghanim, N., et al. 2011, A&A, 536, A23
Planck Collaboration, Ade, P. A. R., Aghanim, N., et al. 2016, A&A, 594, A28
Qian, L., Yao, R., Sun, J., et al. 2020, Innov, 1, 100053
Snell, R. L., Huang, Y. L., Dickman, R. L., & Claussen, M. J. 1988, ApJ, 325, 853
Snell, R. L., Scoville, N. Z., Sanders, D. B., & Erickson, N. R. 1984, ApJ, 284, 176
Tang, N., Li, D., Heiles, C., et al. 2016, A&A, 593, A42
Tang, N.-Y., Zuo, P., Li, D., et al. 2020, RAA, 20, 077
Tatematsu, K., Umemoto, T., Heyer, M. H., et al. 1998, ApJS, 118, 517
Torrelles, J. M., Eiroa, C., Mauersberger, R., et al. 1992a, ApJ, 384, 528
Torrelles, J. M., Gomez, J. F., Anglada, G., et al. 1992b, ApJ, 392, 616
Turner, B. E., Pirogov, L., & Minh, Y. C. 1997, ApJ, 483, 235
Virtanen, P., Gommers, R., Oliphant, T. E., et al. 2020, Nat. Methods, 17, 261
Wang, Y., Bihr, S., Beuther, H., et al. 2020, A&A, 634, A139
Wolfire, M. G., Hollenbach, D., & McKee, C. F. 2010, ApJ, 716, 1191
Wu, Y., Liu, T., Meng, F., et al. 2012, ApJ, 756, 76
Yang, J., Umemoto, T., Iwata, T., & Fukui, Y. 1991, ApJ, 373, 137
Zhang, C.-P., Wang, J.-J., Xu, J.-L., Wyrowski, F., & Menten, K. M. 2014, ApJ, 784, 107
Zhang, C.-P., Xu, J.-L., Li, G.-X., et al. 2021, RAA, 21, 209
Zhang, Q., Hunter, T. R., Brand, J., et al. 2005, ApJ, 625, 864
Zuo, P., Li, D., Peek, J. E. G., et al. 2018, ApJ, 867, 13